Exp Brain Res (1994) 98:401–411

ORIGINAL PAPER

Frederick K.D. Nahm · Anders M. Dale
Thomas D. Albright · David G. Amaral

In vivo microelectrode localization in the brain of the alert monkey: a combined radiographic and magnetic resonance imaging approach

Received: 22 May 1993 / Accepted: 22 October 1993

Abstract A technique is described for in vivo localization of microelectrodes during single-unit recording in the alert monkey. Four hollow glass spheres filled with copper sulfate and iohexol were affixed to the surface of the animal's skull prior to the acquisition of a series of coronal magnetic resonance (MR) images. These reference beads were visible in both X-ray and MR images. Cranial recording chambers were then implanted bilaterally over the amygdaloid complex. A microelectrode was advanced to various depths in the subject's brain. At each selected microelectrode site, five radiographs were obtained and a small electrolytic lesion was made. Based on the data from the radiographs, we computed the position of the microelectrode tip at each site relative to the reference beads. With a precision of 625 μm, this method was used to predict the neuroanatomical location of ten microlesions placed in both subcortical and cortical structures. Postmortem histological analysis revealed that the actual location of the lesions closely matched predictions arrived at using the X-ray/MRI localization technique. This technique thus provides an accurate, reliable and noninvasive method for in vivo localization of microelectrode recording sites.

F.K.D. Nahm · T.D. Albright
The Salk Institute for Biological Studies,
La Jolla, CA 92037, USA

F.K.D. Nahm (✉)
Vision Center Laboratory, The Salk Institute,
P.O Box 85800, San Diego, CA 92186, USA,
FAX no. 619–546–8526, e-mail: Nahm@Fechner.salk.edu

A.M. Dale
Department of Cognitive Science,
University of California San Diego,
La Jolla, CA 92093, USA

D.G. Amaral
Center for Behavioral Neuroscience,
State University of New York Stony Brook,
Stony Brook, NY 11794, USA

Key words Radiography
Magnetic resonance imaging · Microlesion
Single-Unit · Monkey

Introduction

In non-human primate neurophysiological studies, investigators must attempt to identify the location of a recording probe relative to specific brain structures. There are two standard approaches to this problem. The first is predictive in nature and involves guidance by stereotaxic coordinates and/or electrophysiological cues. The second, which is confirmational, involves postmortem analysis of brain tissue. Although both approaches are commonly employed in a single experiment, there are severe limitations associated with each.

Foremost among traditional predictive techniques is the use of a stereotaxic coordinate system. While highly reliable when applied to the brains of many smaller animals, the substantial degree of interanimal variability in the location of brain structures in larger mammalian species, such as macaques, renders ineffective most attempts to target structures on the basis of stereotaxic coordinates alone (Wagman et al. 1975). Alternatively, changes in neuronal activity encountered along microelectrode penetrations may be used as a guide in localizing structures of interest. For a number of brain structures, particularly primary sensory cortical regions, well-defined neurophysiological characteristics provide information sufficient to infer location with reasonable accuracy. When recording from deep brain structures, however, the frequent lack of such precise neurophysiological cues combined with the potential for microelectrode shear makes the problem of localization pervasive.

The standard confirmational approach to localization of brain probes has been postmortem histological analyses to reconstruct probe trajectories from lesion-induced or inadvertent tissue damage. While such procedures generally provide definitive evidence for probe

alignment, they are nonetheless beset by problems of a different kind. Postmortem measurements are untimely since probe location remains unknown until all in vivo experimental procedures are terminated. In long-term neurophysiological experiments the consequences of such a posteriori recognition of probe misplacement can be profound.

In an effort to provide a more sophisticated method for localizing microelectrodes in vivo, we have developed a new technique that combines the imaging features of magnetic resonance (MR) and radiography. Although MR imaging is useful in rendering images of brain structures within the skull (Alvarez-Royo et al. 1991; Rebert et al. 1992), and radiography can be useful in estimating the intracerebral location of a brain probe via its position relative to bony landmarks at the base of the skull (Aggleton and Passingham 1981), neither technique, when used independently, is capable of imaging the position of a brain probe relative to a specific brain structure. The goal of our technique, then, is to render a visual representation of the position of the microelectrode tip relative to brain structures of interest. In an experimental test of this technique, we used it to visualize the locations of a microelectrode relative to a number of cortical and subcortical structures. The accuracy of the technique was verified through the placement of microlesions at identified sites, followed by postmortem histological analysis of brain tissue.

Application of the technique

The in vivo microelectrode localization technique we have developed is designed for neurophysiological protocols involving awake, behaving rhesus monkeys. With appropriate modifications, this technique could be applied to a range of other animal species and/or experimental settings (e.g., neuroanatomical injection studies and neuropsychological lesion studies). Moreover, the equipment and supplies mentioned in the following discussion are recommendations only in that they correspond to those successfully used for experimental validation of this new technique.

Step 1: Construction of reference markers and surgical implantation

The goal of the first step is to construct reference markers which, when implanted rigidly in the skull of the experimental subject, can be used to define identical 3-D coordinate systems in both MRI and X-ray data sets. Hollow glass spheres (Charles S. Rebert, SRI International) with an inside diameter of 2–3 mm are first filled with a solution consisting of 12.5 mg copper sulfate dissolved in 1.0 ml of Omnipaque (iohexol, Sanofi Winthrop Pharmaceuticals), and then sealed with four alternating layers of dental acrylic and cyanoacrylate glue. Copper sulfate is a paramagnetic substance that provides a bright signal in T1-weighted MR images while the radiopacity of iohexol allows the same reference beads to be seen in radiographs.

Because these reference beads are integral to each and every localization attempt, they must be firmly affixed to the cranium of the experimental subject such that they will remain immobile for the duration of the experiment. Using standard aseptic surgical procedures (e.g., Albright et al. 1984), small depressions are made on the surface of the cranium. The filled beads are then anchored in these depressions using dental acrylic for adhesion and protection (Alvarez-Royo et al. 1991; Rebert et al. 1992). Although the precise stereotactical position of these beads is not important, it is essential that the implanted beads be configured so as to minimize their occlusion by one another, as well as any additional cranial implant hardware (see step 3). We recommend that five to six beads be implanted on the skull. A minimum of three beads are needed for relating the 3-D X-ray and MRI cartesian coordinate systems; a fourth bead provides redundancy necessary for detecting errors in the computationally derived position of any one of the beads.

Step 2: Acquisition of MR images

The goal of the second step is to obtain an MRI data base for each experimental subject which is then used to construct an individualized brain atlas. The monkey must first be immobilized for the MR scans with a surgical level of anesthesia. A modified (Plexiglas) stereotaxic headholder should be used for alignment and support of the head. The stereotaxic device must be positioned in the MR scanner such that imaged "sections" are aligned with standard stereotaxic planes.

For the acquisition of MR images, we suggest a sequence consisting of three parallel T1 weighted inversion recovery pulse sequences (TR = 2000, TI = 708, TE = 12, NEX = 2) offset by 1 mm along the axis orthogonal to the plane of section. The MR data collected using the above scanning protocol should be copied onto a storage medium for later transfer to a computer graphics workstation.

Step 3: 3-D reconstruction of brain from 2-D MR images

The goal of the third step is to reconstruct a 3-D MRI data base upon which the computed position of the microelectrode can be superimposed. The previously collected MR images should be transferred to a computer graphics workstation where they are then "reconstructed". In our laboratory, we have used a magnetic tape drive to transfer the MR images to a Silicon Graphics Iris Indigo R4000 where they are then "stacked" by display software written in 'C' using Silicon Graphics GL routines. In this stack, x and y define the mediolateral and dorsoventral axis within the plane of section, respectively, whereas z defines the rostrocaudal axis (i.e., the axis orthogonal to the plane of section). The origins of the x, y and z axes are arbitrary and, in our experiment, they were defined by the MRI machine-based coordinate system. By reconstructing the MRI data base in this manner, the location of any "feature" in a MRI data base (e.g., the center of a reference bead) is defined by specifying an x, y and z coordinate.

Step 4: Acquisition and analysis of X-ray images

The goal of the fourth step is to obtain a series of perspective views of the reference beads and a microelectrode that has been inserted into the brain of the subject. This is accomplished using radiography. We find that a small, portable veterinary X-ray machine (MinXray, Model X803G) is adequate for radiographic imaging of the skull. To limit exposure levels and maximize contrast in the radiographs, we recommend Kodak PDG ultra-detail film and a Kodak X-Omatic cassette (8 in. × 10 in., 20.5 cm × 25.6 cm) fitted with Lanex Regular intensifying screens (rare earth phosphor; green). Under these conditions typical exposure settings are 70 kV, 20 mA, 0.2 s.

During each X-ray imaging procedure, the cranium must be rigidly positioned using an implanted headpost (see below), or similar device. The monkey should be positioned at a distance of approximately 60 cm from the X-ray source. The X-ray film cassette container (which defines the film plane) can be affixed to a wall behind the monkey. The height, distance (approximately 95 cm) and orientation of the X-ray source relative to the film plane should be kept constant for the duration of the X-ray imaging.

In order to obtain a series of perspective projections of the monkey's skull, it is necessary to vary the monkey's angle of rotation relative to the X-ray source. We suggest a series of X-ray images consisting of three prototypical views of the monkey's head: (1) a coronal image, with the monkey directly facing the X-ray source (0 deg); (2) a sagittal image, with the monkey facing either 90 deg to the left or 90 deg to the right of the X-ray source; and (3) a semi-profile image, with the monkey facing 45 deg away from the X-ray source in the direction opposite to that used for the sagittal image. Once the entire series of X-ray images has been developed, each radiograph should be placed on a light box to allow visualization of points of interest. The relative positions of these points in each X-ray image must then be digitized using a digitizing tablet or similar device. The localization attempt for one microelectrode position will thus generate a data base that contains a series of 2-D coordinates specifying the projection of each point in each X-ray image. This data base is the input for the localization strategy described next.

Step 5: Reconstructing the 3-D location of the microelectrode tip

The goal of the fifth step is to reconstruct the 3-D position of a microelectrode tip relative to the reference beads. When a 3-D object is exposed to an X-ray source, the resulting image of any radiopaque region is a 2-D "shadow" or, more precisely, a perspective projection which is recorded on X-ray film. Although the computational problem is decidedly non-trivial, it is possible to reconstruct the 3-D configuration of an object by exploiting the parallax associated with different 2-D perspective projections of the object. The solution to this 3-D reconstruction problem is abetted by the fact that the 3-D coordinates of the features giving rise to a subset of the imaged points (i.e., the reference beads) are known from the MRI data base in advance. The computational strategies that we have employed for solving this problem are presented in the Appendix. The solution that results from the application of these computations is a set of spatial coordinates that define the position of an intracranial microelectrode tip relative to reference beads on the skull.

Step 6: Superimposing X-ray and MR reconstructions

The goal of the sixth and final step in the application of our in vivo localization technique is to determine the MRI-based neuroanatomical feature onto which the computed location of the microelectrode tip maps. The solution that results from step 5 represents a $[x, y, z]$ point within the MRI machine-based coordinate system. The coordinates x and y are used to specify the medio-lateral and dorsal-ventral position of a point within an MR section, respectively, while the z coordinate is used to specify a particular MR section along the AP axis. This point can be graphically depicted by superimposing an icon at the appropriate location in the appropriate MR section. Once accomplished, this information can be used to document the neuroanatomical location from which a cell is recorded. Equally important, this information provides on-line assistance in guiding a microelectrode to other desired recording locations.

Experimental validation of technique

Animal preparation

Subject

One adult female rhesus monkey (*Macaca mulatta*) weighing 6.8 kg was used for experimental validation of the newly developed localization technique. The subject resided unrestrained in her home cage except during the experimental sessions, when the subject was restrained in a standard primate chair. The protocols used in these experiments were approved by the Salk Institute Animal Care and Use Committee and they conform to USDA regulations and NIH guidelines for the humane care and use of laboratory animals.

Surgical preparation and wound maintenance

After a period of acclimation to the primate chair and experimental chamber, the monkey was surgically prepared for neurophysiological recording. Many of the details of our procedures for surgical preparation have been described previously (Albright et al. 1984; Dobkins and Albright 1994). All surgical procedures were performed under strictly aseptic conditions using barbiturate anesthesia (sodium pentobarbital, 25 mg/kg i.v. bolus initially, followed by continuous infusion at a rate of 3.5 mg/kg/h; Hotvedt et al. 1982).

The initial surgery was performed for the purpose of implanting reference "beads" (step 1), which would be visible in both MR sections and X-ray images. Four of these beads were surgically implanted at selected positions on the dorsolateral surface of the skull using dental acrylic for adhesion following the protocol of Alvarez-Royo et al. (1991). After full recovery from the bead implant surgery but prior to the implantation of cranial hardware for neurophysiological recording, three MR scans were obtained (step 2).

A second surgical procedure was performed in order to affix two stainless steel recording chambers and a stainless steel headpost to the skull using stainless steel skull screws, orthopaedic plates (Synthes, Paoli, Pa.), and dental acrylic. The recording chambers (Kopf) were positioned bilaterally over the amygdaloid complex [centered, using coordinates derived from MR sections (see below), at stereotaxic coordinates AP 25 mm, ML 14 mm for the left hemisphere and AP 25 mm, ML 12 mm for the right hemisphere]. A craniotomy measuring approximately 8 mm in diameter was made through the skull in each recording chamber to allow for repeated microelectrode access.

The monkey was given pre- and post-surgical prophylactic antibiotics and post-surgical analgesics. After healing, the cranial wound margin was treated daily by cleansing with sterile saline and 0.3% H_2O_2 and by application of a topical antibiotic (Nitrofurazone, 0.2% in water soluble powder).

Magnetic resonance imaging protocol

Magnetic resonance images were obtained using a 1.5–T GE SIGNA scanner at the UCSD Magnetic Resonance Institute. The monkey was immobilized with an initial bolus of barbiturate anesthetic and subsequently maintained with continuous infusion of the same anesthetic throughout the scanning procedure (see Animal preparation). The monkey was then positioned for collection of MR images according to the procedure outlined in step 2. Using the T1-weighted inversion recovery pulse sequence also described in step 2, a total of 94 coronal MR sections were obtained at 1-mm intervals along the anteroposterior axis. All scans used a 16-cm field of view, a matrix size of 256 × 192, and contiguous 3-mm slices. The images obtained from these scans were stored on magnetic tape and subsequently transferred to a Silicon Graphics workstation for 3-D reconstruction.

Acquisition of X-ray images

X-ray images were obtained using a standard portable veterinary X-ray machine secured on a variable-height moveable platform and following the procedure outlined in step 4. Standard operating procedures were set forth by the Salk Institute Radiation Safety Officer. Exposed film was processed using a Fuji RG II developer.

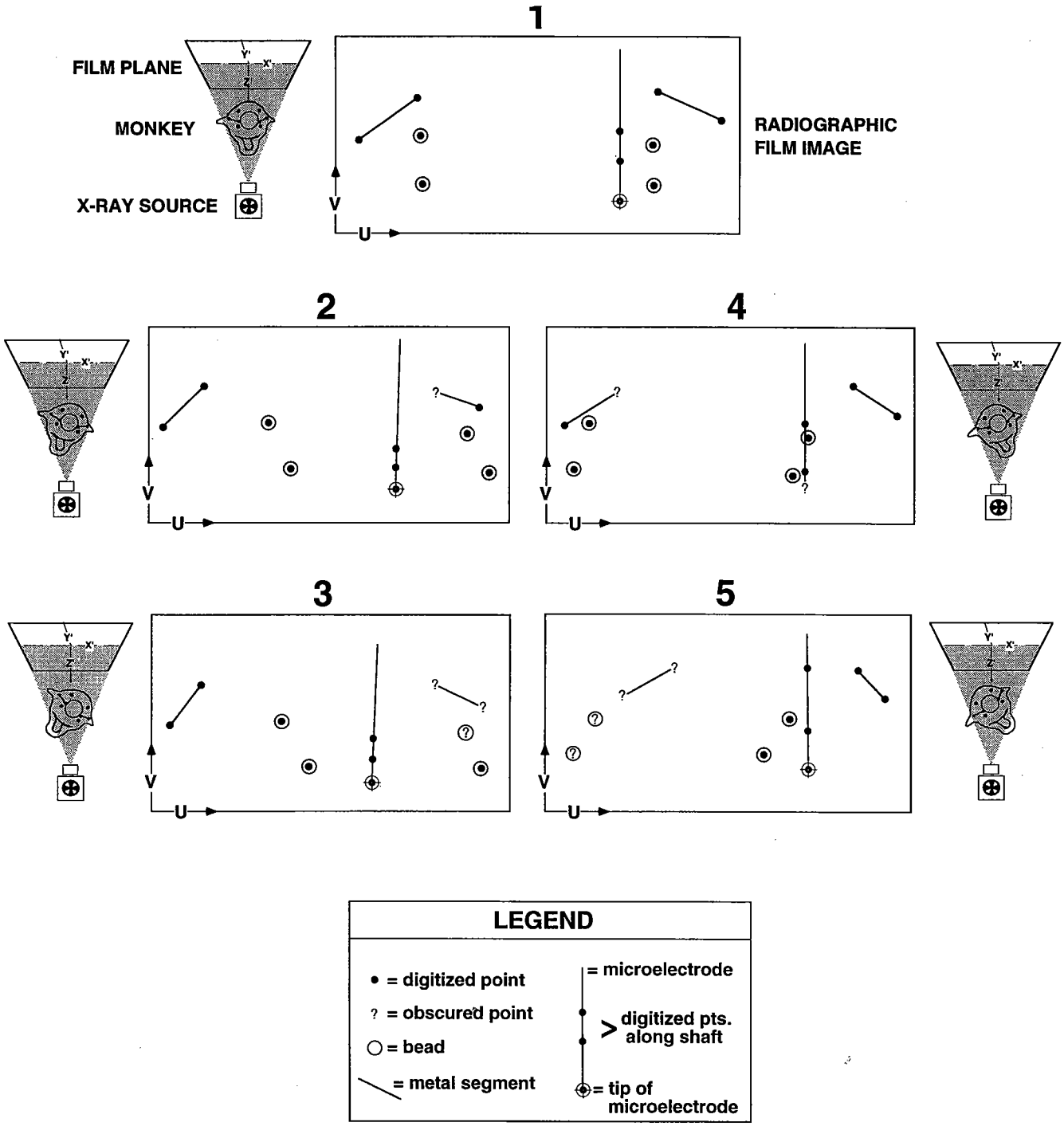

Fig. 1 The boxes labelled 1–5 are digitized representations of five 2-D radiographic film images for case 1. Successfully identified critical points within each radiographic film image 1–5 are represented by *black dots*. A *question mark* represents an occluded point. The coordinate axes within each radiographic image are represented by parameters u and v, whereas the position of the monkey relative to the film plane is referred to by the parameters x', y' and z', with z' directed through the center of the x-ray source. The monkey's angle of rotation relative to the x-ray source for image 1 is 0 deg; for images 2 and 4, −20 and +20 deg, respectively; for images 3 and 5, −40 and +40 deg, respectively. These angles are only estimates; precise knowledge of the angles is not essential for 3-D reconstruction. Atop the monkey's head are shown the locations of the reference beads (*small black dots*) and the extracranial markers (*spherically capped black bars*) relative to the cranial implant graphically depicted by a *circle*. In case 1, only 45 points out of a possible 55 (film 1, $n=11$; film 2, $n=10$; film 3, $n=8$; film 4, $n=9$; film 5, $n=7$) were detectable and available for use in computing the 3-D position of the microelectrode tip due to occlusion by cranial implant hardware or bony structures at the base of the brain

Since the primate chair we used prevented the acquisition of sagittal X-ray images of the monkey's skull, the angles of view differed from those suggested in step 4 (0°±45°, ±90°). Instead, we acquired five X-ray exposures per localization attempt with the monkey facing the X-ray source at the following angles: 0° (monkey directly facing the beam), −20° and −40° (facing left), and +20° and +40° (facing right). This procedure, which is illustrated schematically in Fig. 1, was performed with the microelectrode positioned near a number of selected cortical and subcortical sites. Once the five radiographs were developed, each radiograph was placed on a light box to allow visualization of points of interest.

In order to supplement the information provided by the four surgically implanted beads, two small segments of metal rod (1.5 mm diameter, 17.4 mm long) were affixed to the cranial implant with electrode cream for the duration of each experimental session. The ends of these metal rods provide four additional reference points in each radiographic. These additional reference points are only used for the purpose of 3-D reconstruction from multiple 2-D radiographs. Their precise positions on the cranium were not critical; it was only critical that these positions remained constant for the set of radiographs taken at each microelectrode position. The metal rods were, of course, not present during the MR scans and were, therefore, not critical for the registration of X-ray and MR images. They were removed at the end of each experimental session.

We attempted to identify a total of 11 points on each radiograph: the center of the surgically implanted beads ($n=4$); the endpoints of the two externally mounted metal rods ($n=4$), maximally dispersed points along the microelectrode shaft ($n=2$), and the tip of the microelectrode ($n=1$) (Fig. 1). The relative positions of these 11 reference points were digitized using Sigma Scan software (Jandel Scientific, Sausalito, Calif.) implemented on a PC equipped with a peripheral digitizing tablet (Hitachi, Model HDG-1515B). The digitization of 11 points from a complete X-ray series (five views) generated a data file consisting of 55 data points (i.e., 55 paired x–y coordinates) per microelectrode localization site. While this was the maximum number of data points obtainable from any series of radiographs, the cranial implant (affixed to the skull by radiopaque stainless steel screws) routinely occluded a subset of the potential data points in one or more views.

Localization of microelectrode tip

Based on a series of X-ray images, the location of the tip of a microelectrode at a number of cortical and subcortical sites was determined using the computational strategies described in step 5 and in the Appendix. Using Silicon Graphics GL routines with display software written in C, this point was graphically depicted in the appropriate MR section by crosshairs, the center of which demarked the predicted neuroanatomical locus of the microelectrode tip. A microlesion was placed at each of these localization site for subsequent histological verification.

Electrophysiology and lesion parameters

Paralyene-coated tungsten microelectrodes (Frederick-Haer, Brunswick Me.) with exposed tips of 10 μm or less were used to record extracellular activity from single neurons or small multiunit clusters using conventional electrophysiological techniques (e.g., Albright et al. 1984; Dobkins and Albright 1994). Electrodes were lowered into the brain through a stainless steel guide tube by means of a hydraulic microdrive. The guide tube was lowered through the craniotomy to penetrate the dura and the microelectrode was passed through the guide tube to the desired depth. The microelectrode, guide tube, and microdrive assembly were attached to the recording chamber by way of an x–y stage (Kopf, Tujunga, CA). The x- and y- axes of the stage were aligned with the AP and ML stereotaxic axes, respectively. This arrangement allowed for easy manipulation of the AP or ML location of the microelectrode penetration as required during the course of each experiment.

Small electrolytic lesions were placed at selected cortical and subcortical locations by passing low-level direct current (5–10 μA for 20–30 s) through the recording microelectrode. A total of five microelectrode penetrations were made in the experimental animal on two separate occasions separated by two days; three penetrations were placed in the left hemisphere and two penetrations were placed in the right hemisphere. A minimum of one and a maximum of three lesions were made along each penetration. A total of ten lesions were made.

Histological analysis

Nine days following the last experimental session the subject was deeply anesthetized and perfused transcardially with 10% saline followed by 10% formalin in 0.1 M phosphate buffer (ph 7.2). The brain was exposed and, following 3 days of postfixation in the same fixative, blocked into three pieces in the stereotaxic apparatus. These blocks were each postfixed for 2 days in the same fixative and cryoprotected with 10% glycerol 0.1 M phosphate buffer, followed by 7 days of cryoprotection with 20% glycerol in 0.1 M phosphate. The block containing the microelectrode penetrations was then sectioned at 30 μm on the freezing, sliding microtome. Series 1 and 5 from a one in eight series of sections were immediately transferred to 0.1 M phosphate buffer and subsequently mounted on slides for Nissl staining with thionin. All adjacent series from this block were ultimately mounted for additional validation of microelectrode lesions and complete reconstruction of microelectrode trajectories.

Summary of experimental protocol

Four hollow glass beads were filled with copper sulfate and iohexol, implanted in the skull of one monkey (step 1), and a series of high-resolution coronal MRI sections obtained (steps 2 and 3). Two chronic recording chambers were then implanted over the amygdala. A microelectrode was advanced to various depths in the brain of this subject. At each selected microelectrode site, five radiographs were obtained and a small electrolytic lesion was made. In each radiograph, the centers of the four reference beads, the microelectrode tip, and other points were identified and digitized (step 4). Based on these data, we computed the location of the microelectrode tip in the MRI machine-based coordinate system (steps 5 and 6). This method was used to predict the neuroanatomical location of the microlesions that were placed in both subcortical and cortical structures. The experimental animal was subsequently perfused, postmortem histology performed, and the Nissl-stained sections containing lesions compared to the MRI section that illustrated the predicted lesion site.

Results

A total of ten lesions were made in one experimental animal; data from five of these lesions are presented in detail. The first attempts to localize the microelectrode tip were at each of two sites (case 1 and case 2) along a penetration in the left hemisphere. A microlesion was placed at each of these sites for subsequent histological verification. The localization of case 1 was made at a depth of 18.40 mm (relative to the end of the guide tube). A series of five radiographs was obtained at this depth. In each radiograph, we identified and digitized the locations of the radiographic images of the reference beads ($n=4$), the external markers ($n=4$), the microelectrode

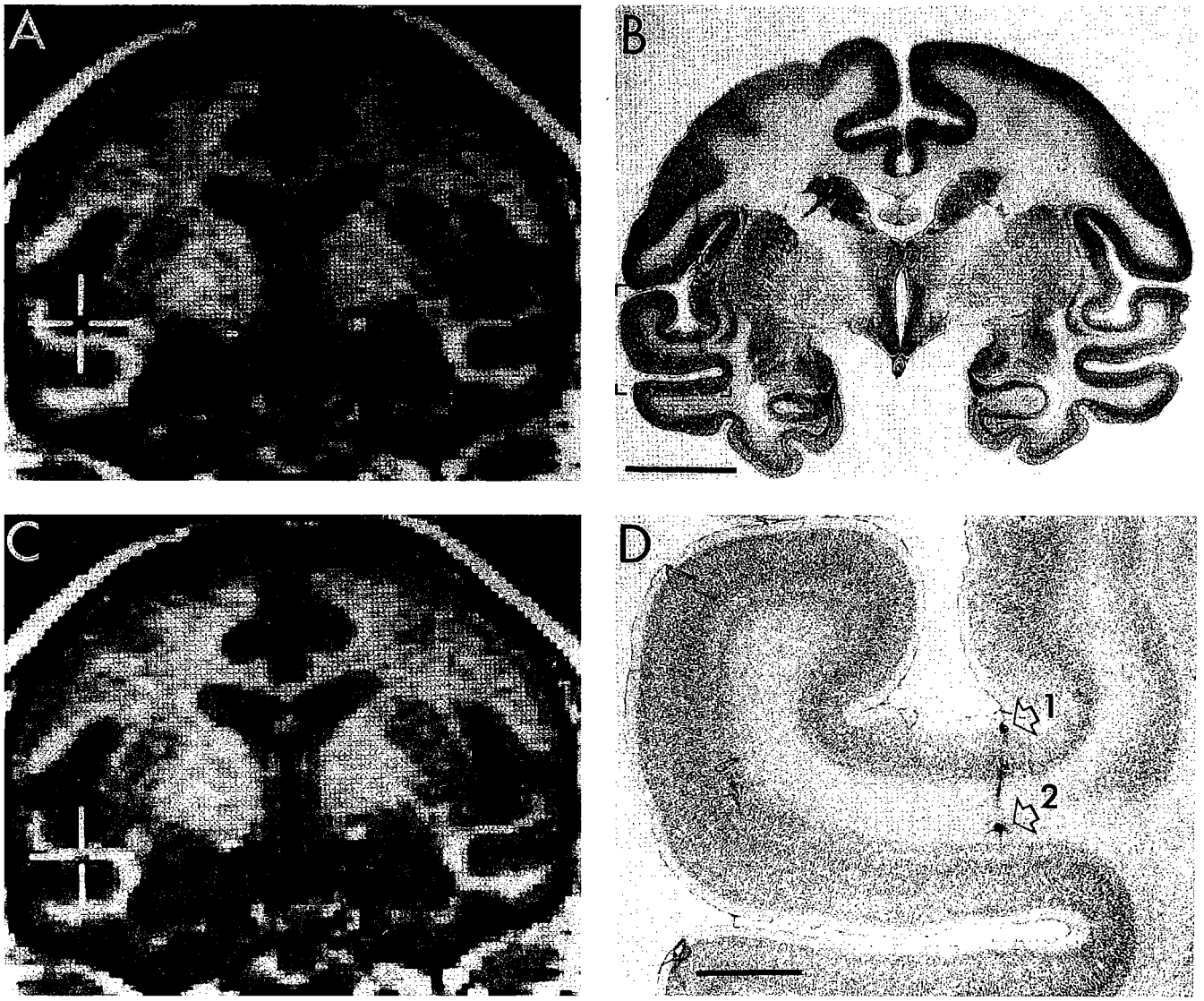

Fig. 2A–D Illustration of the predicted and verified microelectrode positions for cases 1 and 2. **A** A photograph of the appropriate MR section as identified by the in vivo technique for case 1. *Crosshairs* in panel **A** mark the predicted position of the microelectrode tip. **B** A photomicrograph of the Nissl-stained section in which the case 1 microlesion was found. Scale bar, panel **B** equals 10 mm. **C** A photograph of the appropriate MR section for case 2 with the predicted position of the microelectrode marked by *crosshairs*. The case 2 microlesion can be seen in the same Nissl-stained section containing the case 1 lesion (panel **B**). **D** The *bracketed area* in panel **B** at a higher magnification (5×) (*bar* 2 mm). The *arrow* labelled (1) in identifies the case 1 microlesion (predicted by *crosshairs* in panel **A**); the *arrow* labelled (2) identifies the case 2 microlesion (predicted by *crosshairs* in panel C)

tip ($n=1$) and points along the microelectrode shaft ($n=2$). These data are schematically reproduced in Fig. 1.

Crosshairs in panel A of Fig. 2 indicate the x, y and z coordinate within the MRI data base onto which the localized microelectrode tip maps for case 1. From the MR section it can be seen that the predicted microelectrode position is in the superficial laminae of the neocortex in the floor of the lateral fissure. A microlesion was made to enable histological verification of this position. In order to insure that the case 1 lesion was well within an area of tissue (it being rather close to the sulcus), the microelectrode was advanced another 100 μm (relative to the depth at which the tip was localized) and a lesion was made at a depth of 18.50 mm. Thus, the case 1 lesion was placed 100 μm ventral to the computed localization of the microelectrode in case 1. A photomicrograph of the Nissl-stained section in which the case 1 lesion was identified is shown in panel B of Fig. 2. A higher magnification (5×) of this Nissl-stained section is shown in panel D of Fig. 2, with the case 1 lesion identified by the arrow labelled "1". As predicted, the case 1 lesion was located in the superficial layer of the cortex. These data indicate that our in vivo technique was highly accurate in localizing the microelectrode tip for case 1.

The location of the microelectrode tip was determined for a second site (case 2) along the same penetration at a depth of 20.60 mm, 2.2 mm ventral to the com-

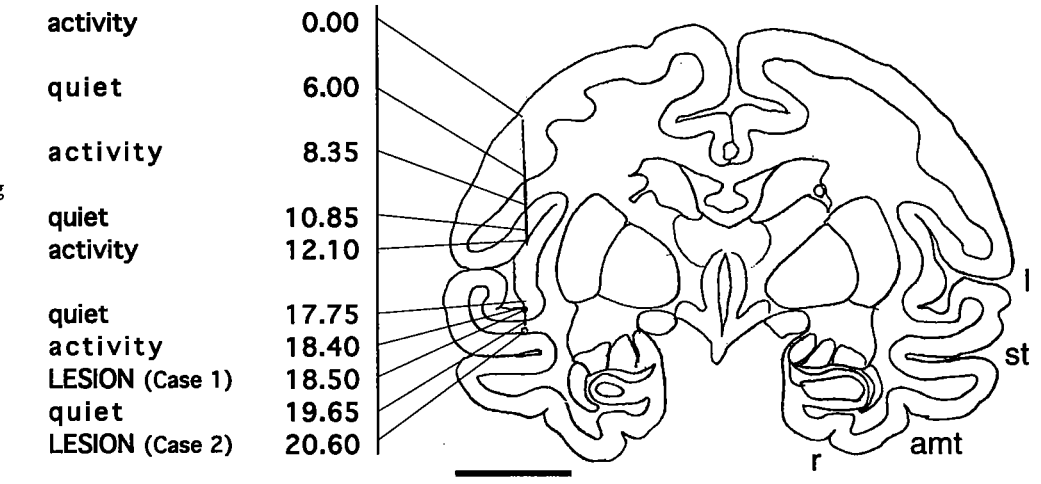

Fig. 3 Camera lucida drawing of a Nissl-stained section showing the microelectrode pass reconstruction from case 1 and case 2. The neurophysiological profile of extracellular multiunit activity is shown at specific depths along this penetration. Scale bar 10 mm. (*l* Lateral sulcus, *st* superior temporal sulcus, *amt* anterior middle temporal sulcus, *r* rhinal sulcus)

puted microelectrode position for case 1. The predicted location of the microelectrode for case 2 is shown on the appropriate MR section in panel C of Fig. 2. This site (indicated by crosshairs) lies, as expected, in the white matter below case 1. The histologically verified position of the case 2 lesion is shown in panel B of Fig. 2, and at a higher magnification in panel D (arrow labelled "2"). The distance between the microelectrode locations in cases 1 and 2 as predicted from our in vivo method was 2.23 mm. Since the microelectrode in case 1 was advanced 100 μm ventral to its predicted site, the corrected distance between the case 1 and 2 microlesions was 2.13 mm. The distance between the two sites as measured from the identified lesions in the Nissl-stained sections was 2.00 mm. These distances (i.e., 2.13 mm and 2.00 mm) differ by approximately 5%, which is consistent with the uncertainty in linear measurements resulting from shrinkage that occurs during Nissl processing methods (Van Essen and Maunsell 1980).

Figure 3 is a camera lucida drawing of the Nissl-stained section in panel B of Fig. 2 showing the microelectrode pass reconstruction from cases 1 and 2. It can be seen from the physiological data (Fig. 3) that at a depth of 17.75 mm, there was little or no neuronal activity. As the microelectrode was advanced an additional 650 μm, to a depth of 18.40 (100 μm dorsal to the case 1 lesion site), we observed an increase in neuronal activity. These data are consistent with the case 1 lesion and the profile of responses predicted by a perpendicular penetration at the medio-lateral level indicated by crosshairs in panel A of Fig. 2. As the microelectrode was further advanced along this penetration, an area of increased neuronal response (indicative of a high density of cell bodies) was encountered immediately below the location of case 1 (Fig. 3). This was followed by an area of minimal neuronal activity, indicative of white-matter and consistent with the neuroanatomy predicted by the relative locations of cases 1 and 2 in the MR data base.

On a second pass in the left hemisphere located rostral to the previous penetration, the microelectrode was advanced to a depth of 8.45 mm and a series of radiographs obtained. (Because the depth of the guide tube varied slightly from one microelectrode penetration to another, the absolute depth measurements are not directly comparable across penetrations.) The predicted location of the microelectrode at this site (case 3) is illustrated in panel A of Fig. 4 by crosshairs superimposed upon the appropriate section. This site lies at the dorsolateral border of the putamen. The histologically verified location of the case 3 lesion can be seen in the Nissl-stained section shown in panel B of Fig. 4. Once again, the predicted and histologically verified microelectrode positions were in close correspondence.

Another microelectrode penetration was made in the right hemisphere, caudal to that described above. The microelectrode was advanced to a depth of 20.00 mm and another series of radiographs obtained. The predicted location of the microelectrode at this depth (case 4) is shown in panel C of Fig. 4 by crosshairs superimposed upon the appropriate MR section. This microelectrode site mapped onto the mid-region of the globus pallidus. The histologically verified location of the case 4 lesion can be seen in the Nissl-stained section shown in panel D of Fig. 4.

Finally, the microelectrode was advanced an additional 10 mm below the depth of case 4 along the same penetration (i.e., to a depth of 30.00 mm) and another series of radiographs obtained. The predicted position of the microelectrode at this more ventral site (case 5) is shown in panel E of Fig. 4 by crosshairs superimposed upon the appropriate MR section. The Nissl-stained section in which the case 5 lesion was found is shown in panel F of Fig. 4. This microelectrode site lies in the most posterior extent of the amygdaloid complex, in the so-called amygdalohippocampal area. This Nissl-stained section lies 210 μm caudal to that shown in panel D of Fig. 4; evidence that the microelectrode was oriented along a posteriorly directed trajectory. The distance between the predicted microelectrode sites for cases 4 and 5, as determined from the in vivo method is 9.52 mm. The distance between the corresponding lesions as measured from the Nissl-stained sections, is

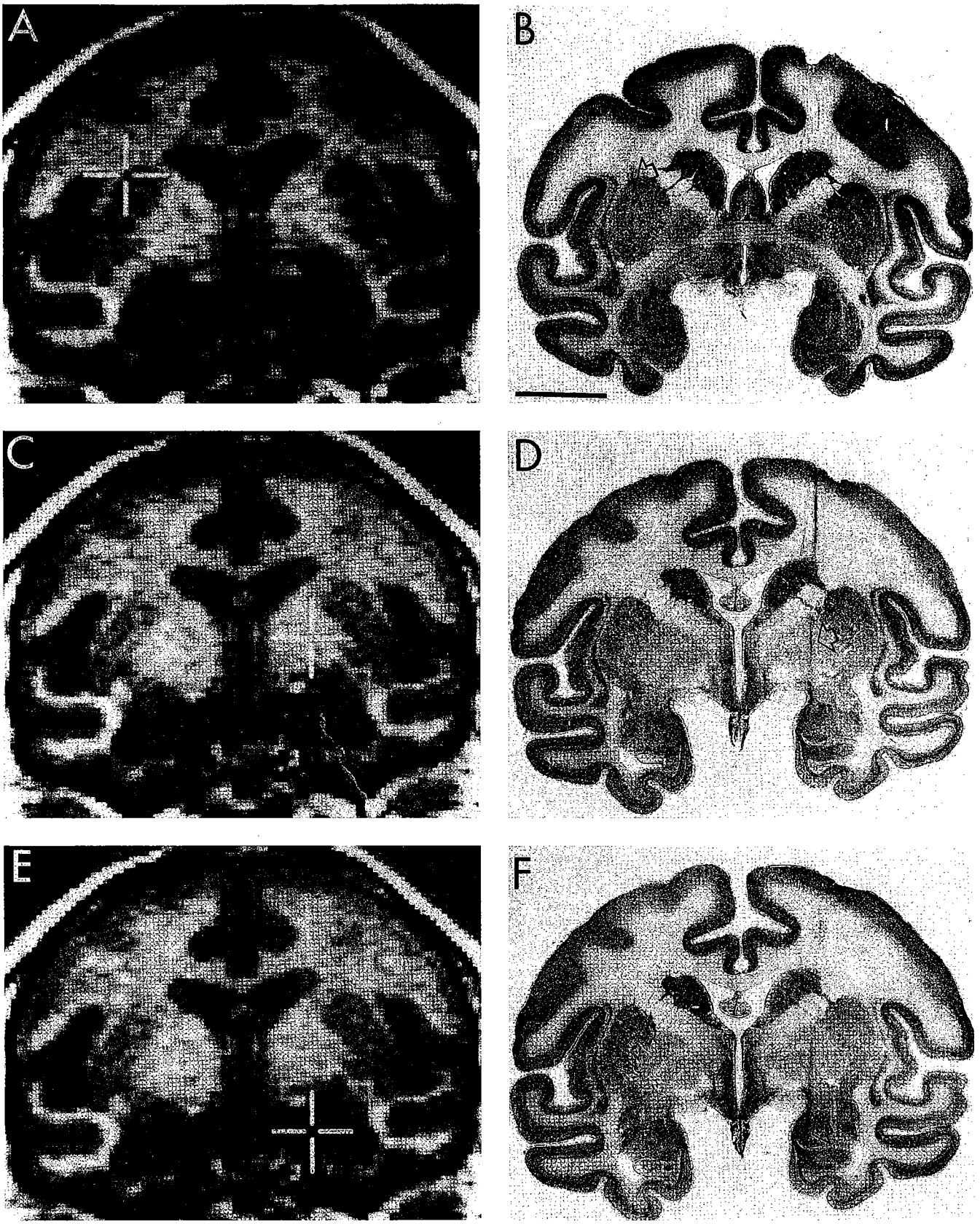

Fig. 4 Predicted and verified microelectrode positions for cases 3, 4 and 5. **A**, **C**, **E** Photographs of the appropriate MR sections as identified by the in vivo technique for cases 3, 4 and 5, respectively. *Crosshairs* in panels **A**, **C** and **E** mark the predicted position of the microelectrode for cases 3, 4 and 5, respectively. **B**, **D**, **F** Photomicrographs of the Nissl-stained sections in which the microlesion (identified by an *arrow*) for cases 3, 4 and 5 were found. Bar in **B**, 10 mm

9.30–9.50 mm. The discrepancy between the distance travelled by the microelectrode (10.00 mm) and that seen in the MR section (9.52 mm) can be accounted for the by fact that the microelectrode trajectory was caudally inclined.

We have reported five cases to illustrate the successful application of this new technique. There were, however, an additional five localization attempts, for which data have not been presented. For two of these attempts along one penetration, postmortem histological examination revealed extensive gliosis along the microelectrode tract which prevented us from clearly identifying the lesions. In the other three localization attempts, which were also made along a single penetration, only one lesion was clearly identifiable upon postmortem histological examination. Nonetheless, despite our inability to verify the accuracy of our microelectrode depth predictions for these five cases, the histologically identified locations of both microelectrode tracts support our general assertion of accuracy since the mediolateral and anteroposterior position of these tracts were entirely consistent with the predicted trajectories of these two penetrations.

Discussion

The in vivo localization technique we have developed provides a reliable method for verifying the neuroanatomical locus of a brain probe during the course of an experimental session. The application of the technique begins by defining a unique coordinate system in an MRI data base of an experimental subject with the use of surgically implanted reference markers. During a neurophysiological recording session, the position of an intracranial microelectrode relative to these same reference markers can be computed using perspective radiographic projections of the subject's skull. Since the reference markers are also present in the MRI data base, the computed microelectrode position directly maps onto a neuroanatomical feature corresponding to the microelectrode recording site. In a first test of this approach, we have managed to identify and visualize the neuroanatomical locus of our probe at various cortical and subcortical sites with a precision of 625 μm. The accuracy of these measurements was successfully confirmed with the aid of microlesions and post-mortem histology. We suggest that this technique be used in the preliminary phases of chronic electrophysiological recording studies to maneuver a microelectrode to the area of interest. Once this is accomplished, microelectrode locations can be verified periodically.

Experimental advantages

Foremost among the advantages afforded by this multimodal technique is the ability to "see" inside the skull. This ability significantly improves the accuracy and reliability of microelectrode placement in neurophysiological recording studies, as well as other procedures in which the position of a deep brain probe relative to a region of the brain must be determined (e.g., neuroanatomical tracer experiments, neuropsychological lesion experiments). In neurophysiological recording studies, for which this technique was developed, an important consequence of this improved accuracy and reliability of microelectrode placement is that the data yield per experimental subject can be increased by delaying, and in some cases obviating, postmortem histological confirmation of recording sites.

Another valuable and convenient feature of this new localization technique is that it lacks dependence upon rigid spatial relationships between the monkey's head, the X-ray source, and the film plane. This is particularly important for experimental preparations involving alert animals, because of the difficulty associated with reliably and repeatedly placing the monkey's skull in a fixed position relative to both the X-ray source and the film plane. By contrast, the recent successful effort by Lemieux et al. (1992) in localizing intracranial EEG electrodes in human subjects using multimodal imaging techniques was facilitated by the fact that the frame coordinates for the two imaging modalities (CT and MR) they employed were stereotactically consistent. In the application of our localization technique, the only fixed measures not subject to optimization are the x, y and z values for each reference bead (directly measured from the MRI data base) and d, the measured distance from the X-ray source to the film plane. The initial estimates for the remaining parameters (e.g., the angles at which the monkey faces the X-ray source) are not crucial, and will only influence the number of iterations required by the algorithm to reach stable solutions.

In the validation of this technique reported here, the spatial resolution within the plane of section was limited only by the resolution of the MR sections (625 μm). This is not, theoretically, the best resolution one can achieve. In preliminary experiments with inanimate objects, we have shown that our numerical approximation techniques for 3-D X-ray reconstruction can be used to estimate the locations of features that resemble the reference beads and microelectrode to within 50–200 μm. The limitation imposed by the resolution of the MRI data base is, however, a more serious problem along the AP axis (i.e., the axis orthogonal to the plane of the MR scans) because the coronal MR sections used in this study were averaged over 3 mm. In practice, this problem could be overcome by acquiring MR sections in three orthogonal planes (coronal, sagittal, horizontal) and mapping the computed 3-D location of the microelectrode onto the appropriate MR section in each of these three planes. An alternative solution to this problem involves the use of volume acquisition and 3-D reconstruction techniques (see Damasio and Frank 1992; Dale and Sereno 1993).

Experimental concerns

Despite the numerous advantages afforded by our in vivo technique, there are a number of procedural concerns that need to be addressed. The first of these is related to the potential for error in estimating coordinates in X-ray images. Since the projections of these points are cast as shadows on the radiographic film, they are subject to the effects of occlusion by bony structures as well as the more frequently encountered problem of occlusion by the cranial implant hardware. Thus, the angles of the head relative to the X-ray source should be carefully chosen so as to maximize the visibility of the microelectrode tip, and minimize the occlusion of the reference beads. However, failure to identify the microelectrode tip and/or reference beads in one or two X-ray images does not present an intractable problem for our technique (indeed, such circumstances are routine), since the problem of localization is, in general, overconstrained (i.e., more equations than unknown parameters, see Appendix).

Once the radiographic image of the reference beads and the microelectrode tip have been identified, the next task is to assign these points numerical coordinates by digitizing their relative positions. Selecting the appropriate part of an image is not difficult for sharply defined features such as the microelectrode tip. By contrast, determining the center of a reference bead in an X-ray image is more difficult because the radiographic appearance of the reference beads is a spherical density gradient. Currently, we have no quantitative solution to this problem; the assignment of numerical coordinates is entirely based on visual inspection. The subjective nature of these measurements is thus a potential source of experimental error. In practice, however, because our technique employs computational strategies that have internal checks for consistency, this potential error cannot seriously effect the final solution to 3-D localization attempts. For example, if a significant error is made in the digitization of the projections of the data points in an X-ray image (e.g., center of reference beads) it will usually result in a high cost function value for the solution (i.e., a high residual variance), and the source of the error can be detected by inspecting the differences between the predicted and measured X-ray projections of each point in each image.

It should be noted that neither the number of views (five) nor the number of points per view (11) used in the present test of this novel localization technique are optimal. The construction of our primate chair prevented us from acquiring X-ray images with the monkey facing 90 deg away from the X-ray source. This restriction necessitated adding extracranial markers to supplement the four implanted beads used in our study.

Future directions

This technique represents a first step toward the development of efficient, inexpensive, and user-friendly techniques for in vivo microelectrode localization. At present, the requirements to implement this technique include a sophisticated graphics workstation capable of rapid display of MR sections, as well as the software for both the 3-D reconstruction and the localization technique. In the near future, we anticipate that these requirements can be met by a reasonably priced computer and a generally applicable set of utilities. The process of acquiring and digitizing X-ray images needs to be streamlined, perhaps by substituting the radiographic film with a CCD that transmits the X-ray image into a computer data base. In parallel, on line in vivo visualization of brain probes could be coupled with microdrive output circuitry in order to "step" the brain probe through graphically reproduced brain images.

Acknowledgements Supported by McDonnell-Pew Center for Cognitive Neuroscience at San Diego grants for graduate and research support (F.K.D.N. and A.D.), the Norwegian Research Council (A.D.), NIH grant HD22614 (A.D.), NEI grant EY07605 (T.D.A.), NIMH grant MH41479 (D.G.A.), and NIH grant S15 MH50811 (D.G.A.). We wish to thank Gene Stoner, Lisa Croner, Alexander Pouget, and Marty Sereno for helpful discussions and comments on the manuscript. We are also grateful to Jennifer Costanza for superb technical assistance.

Appendix

The problem of reconstructing the 3-D location of the microelectrode can be stated in the following way. Given the 2-D perspective projections of each of n different points (e.g., reference beads, microelectrode tip, etc.) in each of m different X-ray images, and the locations of a subset of the points (e.g., the implanted beads) in the 3-D MRI coordinate system, determine the 3-D locations of the remaining points (e.g., the microelectrode tip) in the MRI-based coordinate system.

Let $p_j=(x_j, y_j, z_j)$ denote the location of the j^{th} point in the MRI coordinate system, and let $q_{i,j}=(u_{i,j}, v_{i,j})$ denote the 2-D location of the projection of the j^{th} point in the i^{th} X-ray image, with u and v axes parallel to the horizontal and vertical axes of the film, respectively (Fig. 1). To facilitate the analysis, it is convenient to introduce an X-ray-based 3-D coordinate system, with x and y axes in the plane of the X-ray film, parallel to the u and v axes of the film, respectively, and z axes going through the X-ray source (see Fig. 1). To avoid confusion with the MRI coordinate system, we will indicate 3-D X-ray based coordinates by a prime, e.g. $p'_{i,j}=(x'_{i,j}, y'_{i,j}, z'_{i,j})$ is the location of the j^{th} point in X-ray-based coordinates in the i^{th} projection configuration. Using elementary geometry we see that the X-ray projections $q_{i,j}=(u_{i,j}, v_{i,j})$ of a point $p'_{i,j}=(x'_{i,j}, y'_{i,j}, z'_{i,j})$ is

$$u_{i,j} = s_i + \frac{d_i * x'_{i,j}}{d_i - z'_{i,j}} \quad \text{and} \quad v_{i,j} = t_i + \frac{d_i * y'_{i,j}}{d_i - z'_{i,j}} \qquad (1)$$

where d_i is the distance from the X-ray film to the X-ray source in the i^{th} projection configuration; s_i and t_i are

the x' and y' offsets of the u and v coordinates, respectively.

Since both the MRI-based and the X-ray based 3-D coordinate systems are assumed to be right-handed cartesian ones, the transformation from one to the other involves only rigid translation and rotation, which can be expressed as

$$x'_{i,j} = a_i + x_j(\cos\beta_i \cos\gamma_i - \sin\alpha_i \sin\beta_i \sin\gamma_i) - y_j \cos\alpha_i \sin\gamma_i + z_j(\cos\gamma_i \sin\beta_i + \cos\beta_i \sin\alpha_i \sin\gamma_i) \quad (2)$$

$$y'_{i,j} = b_i + x_j(\cos\gamma_i \sin\alpha_i \sin\beta_i + \cos\beta_i \sin\gamma_i) + y_j \cos\alpha_i \cos\gamma_i + z_j(\sin\beta_i \sin\gamma_i - \cos\beta_i \cos\gamma_i \sin\alpha_i) \quad (3)$$

$$z'_{i,j} = c_i - x_j \cos\alpha_i \sin\beta_i + y_j \sin\alpha_i + z_i \cos\alpha_i \cos\beta_i \quad (4)$$

where a_i, b_i and c_i are translations in x', y' and z', respectively; and α_i, β_i and γ_i are angles of rotation around the x, y and z axes, respectively. Equations 1–4 provide an explicit formula for calculating the X-ray projection $q_{i,j}=(u_{i,j}, v_{i,j})$ of any point $p_j=(x_j, y_j, z_j)$ in the MRI coordinate system given the projection parameters d_i, s_i, t_i, a_i, b_i, c_i, α_i, β_i, γ_i.

If the projection parameters could be exactly determined and the points in the X-ray images measured with infinite precision, we could directly solve for the MRI location of the microelectrode tip based on two perspective X-ray images. However, in practice, some of the projection parameters, such as translations a_i, b_i and c_i, and angles of rotation α_i, β_i and γ_i are difficult to control with a sufficient degree of accuracy. An error of just a few degrees of orientation of the monkey's head in the MRI machine relative to the orientation in the X-ray apparatus could introduce errors of several millimeters in the localization of the points. It is therefore necessary to be able to derive the values of these parameters, as well as the locations of the points, from the the measured X-ray projections.

A general way of posing such non-linear inverse problems is in terms of optimizing a so-called cost function. A natural choice of cost function H is the average squared distance between the observed and predicted X-ray projections,

$$H(\Theta) = \frac{\sum_i^m \sum_j^n w_{i,j}((u_{i,j} - \hat{u}(\Theta_{i,j}))^2 + (v_{i,j} - \hat{v}(\Theta_{i,j}))^2)}{\sum_i^m \sum_j^n w_{i,j}} \quad (5)$$

where Θ is a vector of all known and unknown parameters (i.e., MRI coordinates of each point, and projection parameters for each image); $\Theta_{i,j}$ refers to the vector $(x_j, y_j, z_j, d_i, s_i, t_i, a_i, b_i, c_i, \alpha_i, \beta_i, \gamma_i)$ of parameters in Θ specifying the MRI coordinates of the j^{th} point and the projection parameters for the i^{th} image; $u_{i,j}$ and $v_{i,j}$ are the observed X-ray projections of the j^{th} point in the i^{th} image, and $\hat{u}(\Theta_{i,j})$ and $\hat{v}(\Theta_{i,j})$ are the corresponding predicted X-ray projections given the parameter vector $\Theta_{i,j}$ and the forward expressions in (1) through (4); and $w_{i,j}$ is a binary variable taking on the value 1 if the projection of the j^{th} point in the i^{th} image is observed (i.e., not occluded), and 0 otherwise. Although no explicit expression exists for the parameter vector Θ which minimizes Eq. 5, a wide range of numerical techniques can be used (Press et al. 1988). We have found that a simple gradient descent algorithm works well, although more rapid convergence can be obtained using more advanced techniques.

References

Aggleton JP, Passingham RE (1981) Stereotaxic surgery under X-ray guidance in the rhesus monkey, with special reference to the amygdala. Exp Brain Res 44:271–276

Albright TD, Desimone R, Gross CG (1984) Columnar organization of directionally selective cells in visual area MT of the macaque. J Neurophysiol 51:16–31

Alvarez-Royo P, Clower RP, Zola-Morgan S, Squire LR (1991) Stereotaxic lesions of the hippocampus in monkeys: determination of surgical coordinates and analysis of lesions using magnetic resonance imaging. J Neurosci Methods 38:223–232

Dale AM, Sereno MI (1993) Improved localization of cortical activity by combining EEG and MEG with MRI cortical surface reconstruction: a linear approach. J Cogn Neurosci 5:2 162–176

Damasio H, Frank R (1992) Three-dimensional in vivo mapping of brain lesions in humans. Arch Neurol 49:137–143

Dobkins KR, Albright TD (1994) What happens if it changes color when it moves? Neurophysiological experiments on the nature of chromatic input to macaque visual area MT. J Neurosci (in press)

Hotvedt R, Platou ES, Koppang ER, Refsum H (1982) Pentobarbital plasma concentrations and cardiac electrophysiology during prolonged pentobarbital infusion anaesthesia in dogs. Acta Anaesthesiol Scand 26:638–642

Lemieux L, Lester S, Fish D (1992) Multimodality imaging and intracranial EEG display for stereotactic surgery planning in epilepsy. Electroencephalogr Clin Neurophysiol 82:399–407

Press WH, Flannery BP, Teukolsky SA, Vetterling WT (1988) Numerical recipes in C. Cambridge University Press, Cambridge, UK

Rebert CS, Hurd RE, Matteucci MJ, De LaPaz R, Enzmann DR (1992) A procedure for using proton magnetic resonance imaging to determine stereotaxic coordinates of the monkey's brain. J Neurosci Methods 39:109–113

Van Essen DC, Maunsell JHR (1980) Two-dimensional maps of the cerebral cortex. J Comp Neurol 191:255–281

Wagman JH, Loeffler JR, McMillan JA (1975) Relationship between growth of brain and skull of *Macaca mulatta* and its importance for the stereotaxic technique. Brain Behav Evol 12:116–134